8^{th} International Conference on Numerical Ship Hydrodynamics
Busan, Korea, Sept.22-25, 2003

Moving Towards High-Fidelity RANS Calculations Of Maneuvering Surface Vessels Using Unstructured Grids

Clarence O. E. Burg
Computational Simulation and Design Center
Mississippi State University
burg@erc.msstate.edu

David L. Marcum
Computational Simulation and Design Center
Mississippi State University
marcum@erc.msstate.edu

ABSTRACT

Simulations of maneuvering surface ships using high-fidelity viscous computational fluid dynamics requires the capability to model the conservation of mass and momentum via the unsteady Reynolds-averaged Navier-Stokes, along with appropriate turbulence modeling, the capability to rotate and deflect appendages, accurate force and moment predictions and robust and efficient unsteady nonlinear free surface capabilities. Simulations of flow around transom sterns for naval combatants introduces additional complexities due to grid generation issues arising from wetted or unwetted conditions. Finally, to simulate flow for fully-appended configurations with struts, rudders, shafts and propellers, unstructured grids offer much promise due to the geometric complexities. In this research, a three-dimensional unstructured mixed-element flow solver of the incompressible Reynolds-averaged Navier-Stokes equations with various turbulence models and nonlinear free surface capabilities is studied with the goal of addressing some preliminary issues for rudder-induced, propeller driven, six-degree-of-freedom maneuvers. The research presented herein is divided into three topics, each focused on numerical simulations of the DTMB Model 5415 series hullform. The first topic concerns the accuracy of the free surface and of the forces and moments generated by the unstructured flow solver. Results from a grid refinement study is used to determine the level of grid refinement that are required for accurate predictions of the forces and moments for this code. The second topic covers two different types of steady-state maneuvers, the constant drift case and the constant turn case. Flow around the Model 5415 hullform at drift angles from 1 to 5 degrees are presented, as well as flow for turns of constant radius ranging from 6 to 24 ship lengths. The third topic is a prescribed maneuver for the model 5415 hullform with a linear free surface. Simulation data from a rudder-induced, propeller-driven maneuver with no free surface (i.e., the free surface was a symmetry plane) is used to prescribe a maneuver for the Model 5415 hullform. Due to the complexities of moving the grid at each time step, only a linear free surface was used, so that the grid movement algorithm is ignored.

NOMENCLATURE

Y	Free surface elevation
$\vec{u}$	Velocity (u,v,w)
a_t	Grid speed (velocity) $-(V_x,V_y,V_z)$
χ	U-MUSCL parameter
P	Pressure
Fr	Froude number $\frac{U_\infty}{\sqrt{gL}}$
β	Artificial compressibility coefficient
Q	Vector of flow variables
$\vec{F}$	Inviscid flux vector
$\vec{G}$	Viscous flux vector
τ_{ij}	Viscous stresses
$\hat{n}$	Outward pointing unit normal to face
$\hat{n}_{fs}$	Normal at free surface
$\vec{r}$	Vector along edge between two nodes
A	Inviscid flux Jacobian matrix
R	Matrix of right eigenvectors of A
Λ	Diagonal matrix of eigenvalues of A
W	Characteristic variables
ϕ_j	Finite element weight function
γ	Free surface velocity restriction coeff.

INTRODUCTION

Modeling the free surface generated by surface ships and by submerged vessels near the water surface is important for proper understanding of the flow around these vessels. In particular, the free surface changes the resistance of the vessels through the water by changing the pressure distribution and the wetted surface area. The free surface affects the location and magnitude of the vortices that originate from various locations, including the bow, appendages and propulsors, which can greatly affect the performance of the propulsors. The wave signatures of ships and submarines is also of importance. Surface vessels under investigation by ship designers attempt to mitigate the negative influences of the free surface interaction on cavitation, power requirements and wave signature and attempt to use the free surface to improve the performance in other ways. In addition to the ship cruising straight and level, the effects on the ship's performance caused by maneuvering through a change in direction, or through various sea states, especially in regards to wave signature, sea-keeping and cavitation in littoral water are important in the designs and can not be readily tested by experiment.

A long-term goal of the research into numerical simulations is to develop the ability to study the performance of a full ship design, including the interactions of the various appendages, sonar domes, rudders, shafts and propulsors, as the ship maneuvers in response to changes in the settings of the rudders and propulsors. To accomplish this goal, efficient and accurate free surface simulations are needed. Other necessary components to achieve this goal include capabilities to monitor the onset of incipient cavitation, to perform simulation of several vessels in motion relative to one another and to adapt the grid to capture vortices in the water.

Currently, the implicit unstructured code being developed by researchers in the Computational Simulation and Design Center at Mississippi State University solves the three-dimensional, incompressible Navier-Stokes equations, using an edge-based, flux-differencing finite volume method with Roe-averaged variables. The unstructured flow solver was successfully parallelized (Hyams, 2000a), and the code has been ported to a wide variety of high-performance machines. The unstructured grid generator (Marcum, 1998) has the capability of building highly stretched high-aspect ratio grids near viscous surfaces, which include higher order elements such as pyramids and prisms, and allows the flow solver to fully resolve boundary layer features. The unstructured flow solver is also capable of rotating the propulsors and deflecting the rudder appendages. And in conjunction with the grid generator, the flow solver can simulate flow at full-scale Reynolds number, with $y+$ values on the order of 1.0.

At each time step, the nonlinear free surface algorithm solves the kinematic free surface equation

$$\frac{\partial Y}{\partial t} + (u - V_x)\frac{\partial Y}{\partial x} - (v - V_y) + (w - V_z)\frac{\partial Y}{\partial z} = 0 \quad (1)$$

where $Y = Y(x,z,t)$ is the free surface defined as a single-valued function over the xz plane, (u,v,w) are the velocity components in the coordinate directions and (V_x,V_y,V_z) are the grid velocities. A flow-through boundary condition for the free surface based on characteristic variable boundary conditions is used, with the pressure on the free surface set to $P = \frac{Y}{Fr^2}$ where P is the pressure and Fr is the Froude number. After several time steps, the grid is moved to match the free surface while conforming to the geometry, using a three dimensional extension of Farhat's torsional spring method (Farhat, 1998). This grid movement algorithm is quite robust, allowing for moderate to extreme distortions as required by the free surface simulations. As the solution converges, the flow along the free surface becomes tangent to the free surface, and the nonlinear free surface solution is obtained.

Much of this work is an extrapolation of the free surface algorithm used within the three-dimensional structured code UNCLE also developed at Mississippi State University. Beddhu (1994) developed the structured free surface solver, using a modified artificial compressibility formulation. This algorithm was applied to steady and unsteady flow around the Wigley hull (Beddhu, 1998a), to the barehull model 5415 series hull (Beddhu, 1998b), to the Series 60 $C_B = 0.6$ ship (Beddhu, 1998c) and to a more detailed stern analysis for the DTMB Model 5415 series hull (Beddhu, 1999), and further results from simulations of this hullform were presented at the Gothenburg conference (Beddhu, 2000). Initial verification and validation exercises of the unstructured nonlinear free surface algorithm has been presented (Burg, 2002a), which includes a grid refinement study for flow over a submerged NACA0012 hydrofoil, flow around inviscid and viscous Wigley hulls, and flow around the barehull DTMB Model 5415 series hull. More complicated free surface simulations around the DTMB Model 5415 series hull with rudders, shafts, struts and propulsors have been attempted (Burg, 2002b), demonstrating the need for complicated gridding technology and the successful simulation of a rotating propulsor near a nonlinear free surface.

In this paper, the barehull DTMB Model 5415 series hullform will be analyzed exclusively. The primary goal of this work is demonstrate that the nonlinear free surface capabilities within the unstructured flow solver are adequate for simulations of moderate turns into the flow of approximately 5 degrees.

Force comparisons for several different angles of yaw and for several different turning radii are presented, as well as force comparisons and free surface comparisons for a grid refinement study. Finally, a prescribed maneuver with a quasi-linear free surface is performed, using the grid that was moved to match the free surface for the converged steady-state straight level simulation.

In the next section, the Navier-Stokes solution algorithm is reviewed. Then, the free surface algorithm is presented, which includes the method for solving the kinematic free surface equation, the imposition of the hydrostatic pressure on the Navier-Stokes equations and the grid movement algorithm. Finally, the results for the DTMB Model 5415 series simulations are presented.

NAVIER-STOKES SOLUTION ALGORITHM

Three different sets of equations are solved in the process of simulating the flow around surface vessels and submerged vessels near the water surface. The unsteady incompressible Reynolds-averaged Navier-Stokes equations, which are presented here in Cartesian coordinates and in conservative form, are solved to determine the velocity and pressure within the computational domain. Several turbulence models are available including the one-equation Spalart-Allmaras turbulence model, and $q-\omega$, $k-\varepsilon$ and $k-\omega$ two-equation turbulence models, to simulate the turbulent viscosity primarily within the boundary layer, and the kinematic free surface equation is solved to advance the free surface in time.

Governing Equations

Assuming that gravity acts in the y-direction (i.e., the vertical direction), the incompressible Navier-Stokes equations can be expressed in dimensional form, denoted with superscript *, as

$$\begin{aligned} \nabla\cdot(\vec{u}^*) &= 0 \\ \frac{\partial u^*}{\partial t^*}+\nabla\cdot(u^*\vec{u}^*)+\frac{\partial}{\partial x^*}\left(\frac{P^*}{\rho_\infty}\right) &= \mu^*\nabla^2 u^* \\ \frac{\partial v^*}{\partial t^*}+\nabla\cdot(v^*\vec{u}^*)+\frac{\partial}{\partial y^*}\left(\frac{P^*}{\rho_\infty}+gy^*\right) &= \mu^*\nabla^2 v^* \\ \frac{\partial w^*}{\partial t^*}+\nabla\cdot(w^*\vec{u}^*)+\frac{\partial}{\partial z^*}\left(\frac{P^*}{\rho_\infty}\right) &= \mu^*\nabla^2 w^* \end{aligned} \tag{2}$$

The variables in the preceding equation are normalized with respect to a characteristic length scale (L) and free stream values of velocity (U_∞), density (ρ_∞), and viscosity (μ_∞). Thus, the Reynolds number is defined as $Re = U_\infty L/\nu_\infty$. Pressure is normalized with $P = (P^* + \rho_\infty g y^* - P_\infty)/\rho_\infty U_\infty^2$, where P^* is the local dimensional static pressure. Following (Chorin, 1967), an artificial time derivative term ($\partial\rho_a/\partial t$, where $\rho_a = P/\beta$) has been added to the continuity equation to cast the complete set of governing equations into a time-marching form. The nondimensionalized equations can be written in integral form as

$$\frac{\partial}{\partial t}\int_\Omega Q dV + \int_{\partial\Omega}\vec{F}\cdot\hat{\vec{n}}dA = \frac{1}{Re}\int_{\partial\Omega}\vec{G}\cdot\hat{\vec{n}}dA \tag{3}$$

where $\hat{\vec{n}}$ is the outward pointing unit normal to the control volume V. The vector of dependent variables and the components of the inviscid and viscous flux vectors are given as

$$Q = \begin{bmatrix} P \\ u \\ v \\ w \end{bmatrix} \tag{4}$$

$$F\cdot\hat{\vec{n}} = \begin{bmatrix} \beta(\Theta - a_t) \\ u\Theta + \hat{n}_x P \\ v\Theta + \hat{n}_y P \\ w\Theta + \hat{n}_z P \end{bmatrix} \tag{5}$$

$$G\cdot\hat{\vec{n}} = \begin{bmatrix} 0 \\ \hat{n}_x\tau_{xx} + \hat{n}_y\tau_{xy} + \hat{n}_z\tau_{xz} \\ \hat{n}_x\tau_{yx} + \hat{n}_y\tau_{yy} + \hat{n}_z\tau_{yz} \\ \hat{n}_x\tau_{zx} + \hat{n}_y\tau_{zy} + \hat{n}_z\tau_{zz} \end{bmatrix} \tag{6}$$

where β is the artificial compressibility parameter (typically 15 in this work), u, v, and w are the Cartesian velocity components in the x, y, and z directions, and $\hat{n}_x$, $\hat{n}_y$, and $\hat{n}_z$ are the components of the normalized control volume face vector. Θ is the velocity normal to a control volume face:

$$\Theta = \hat{n}_x u + \hat{n}_y v + \hat{n}_z w + a_t \tag{7}$$

where the grid speed $a_t = -(V_x\hat{n}_x + V_y\hat{n}_y + V_z\hat{n}_z)$. The control volume face velocity is given by $\vec{V}_s = V_x\hat{i} + V_y\hat{j} + V_z\hat{k}$. The viscous stresses given in Equation (6) are

$$\tau_{ij} = (\mu + \mu_t)\left(\frac{\partial u_i}{\partial x_j} + \frac{\partial u_j}{\partial x_i}\right) \tag{8}$$

where μ and μ_t are the molecular and eddy viscosities, respectively.

Numerical Approach for Navier-Stokes Equations

The baseline flow solver is a node-centered, finite volume, implicit scheme applied to general unstructured grids with nonsimplical elements, such as prisms and pyramids. The flow variables are stored at the vertices, and surface integrals are evaluated on the median dual surrounding each of these vertices. The nonoverlapping control volumes formed by the median dual completely cover the domain, and form a mesh that is dual to the elemental grid. Thus, a one-to-one mapping exists between the edges of the original grid and the faces of the control volumes. The solution algorithm consists of the following basic steps: reconstruction of the solution states at the control volume faces, evaluation of the flux integrals for each control volume, and the evolution of the solution in each control volume in time.

Reconstruction

A higher order spatial method is constructed by extrapolating the solution at the vertices to the faces of the surrounding control volume. The unweighted least squares method (solved via QR factorization (Anderson, 1994)) is used to compute the gradients at the vertices for the extrapolation, which is similar to a central difference approximation to the gradient. With these gradients known, the variables at the interface are computed using the newly-developed Unstructured MUSCL (U-MUSCL) scheme,

$$Q_f = Q_i + \frac{\chi}{2}(Q_j - Q_i) + (1-\chi)\nabla Q_i \cdot \frac{\vec{r}}{2} \qquad (9)$$

where Q_f is the value at node i side of the face between nodes i and j, χ is a parameter that works the same as the parameter within the MUSCL-approach, and $\vec{r}$ is a vector that extends from node i to node j associated with the control volume face in question. When $\chi = 0$, the more common formulation for the variable extrapolation within unstructured codes is achieved. When $\chi = 1/2$, the error of the extrapolation at the face is minimized for uniform, one-dimensional flow. In all of the simulations reported herein, this parameter is set to $1/2$. For many simulations, this choice of χ allows for a more stable simulation which does not need any limiters, and produces a solution whose residual has been converged to machine zero.

Spatial Residual

The evaluation of the discrete residual is performed separately for the inviscid and viscous terms given in Equation (3). The Roe scheme (Roe, 1981) is used to evaluate the inviscid fluxes at each face of the control volumes. The algebraic flux vector is replaced by a numerical flux function, which depends on the reconstructed data on each side of the control volume face:

$$\Phi = \frac{1}{2}(F(Q_L) + F(Q_R)) - \frac{1}{2}\tilde{A}(Q_R - Q_L) \qquad (10)$$

where $\tilde{A} = \tilde{R}\tilde{\Lambda}\tilde{R}^{-1}$. The matrix R is constructed from the right eigenvectors of the flux Jacobian, and $\tilde{\Lambda}$ is a diagonal matrix whose entries contain the absolute values of the eigenvalues of the flux Jacobian (Taylor, 1991). The matrix $\tilde{A}$ is evaluated with Roe-averaged variables, which is simply the arithmetic average between left and right solution states in the case of incompressible flows.

For general element grids, it is expedient to use only edge-local information to compute the viscous fluxes, which allows the evaluation of viscous fluxes on each face of the control volume without regard to the varying element types of the mesh. An algorithm in which no element information is used outside of metric computations is termed a "grid transparent" algorithm (Haselbacher, 1999). To this end, the viscous fluxes are evaluated directly at each edge midpoint using separate approximations for the normal and tangential components of the gradient vector to construct the velocity derivatives . Using a directional derivative along the edge to approximate the normal component of the gradient and the average of the nodal gradients to approximate the tangential component of the gradient leads to the following expression (Hyams, 2000b):

$$\nabla Q_{ij} \approx \overline{\nabla Q} + \left[Q_j - Q_i - \overline{\nabla Q}\cdot\vec{r}\right]\frac{\vec{r}}{|\vec{r}|^2} \qquad (11)$$

where $\overline{\nabla Q}$ is the average of ∇Q_i and ∇Q_j. As stated above, the weighted least squares method is used to evaluate the nodal gradients in the preceding formula.

Solution Procedure

The temporal derivative is discretized so that either a first or second-order time discretization is available. The resulting system of discretized governing equations is solved via a bi-directional Gauss-Seidel algorithm, which splits the matrix into a diagonal, upper triangular and lower triangular parts and using subiterations to converge the solution at each time step (Hyams, 2000b) (Burg, 2002b).

Boundary Conditions

Three different boundary conditions are used within the free surface simulations: viscous wall (i.e., no-slip) boundary conditions, farfield boundary conditions and free surface boundary conditions, each of

which are handled implicitly. Viscous conditions are enforced by modifying the linear system such that no change is allowed in the velocity, and the pressure is driven according to the imbalance in the continuity equation in the boundary control volume (Anderson, 1994). Farfield conditions are handled via a characteristic variable reconstruction. The free surface boundary conditions will be presented below - in essence, at steady-state, the velocity is tangent to the free surface (i.e., $\vec{u} \cdot \hat{n}_{fs} = 0$) and the pressure is $P = \frac{Y}{Fr^2}$, where Y is the elevation of the free surface above the undisturbed waterline and the Froude number is $Fr = \frac{U_\infty}{\sqrt{gL}}$.

Turbulence Modeling

Both the one-equation turbulence model of Spalart and Allmaras (Spalart, etal, 1992) and the $q-\omega$ (Coakley, 1985), the $k-\varepsilon$ and the $k-\omega$ two-equation turbulence models are available within the solver. Constants are taken from the version II $q-\omega$ model given in (Coakley, 1985). The $k-\varepsilon$ and $k-\omega$ turbulence models have been newly incorporated within the unstructured flow solver. For the simulations presented herein, the one-equation turbulence model of Spalart-Allmaras is used.

The diffusive terms in both turbulence models are discretized in the same manner as the viscous terms for the mean flow, and the convective terms are computed via pure upwinding. Appropriate consideration is given to maintain positive operators in the formation of the Jacobian matrix for the implicit solution of the transport equation(s). The respective turbulence models are incorporated with the mean flow solution in a "loosely-coupled" procedure; that is, the core governing equations are solved first, then the turbulence model is solved independently. This procedure allows for easy interchange of the turbulence models.

NONLINEAR FREE SURFACE ALGORITHM

A nonlinear free surface is obtained for a steady-state simulation by solving the kinematic free surface boundary condition at each time level and imposing the hydrostatic pressure distribution based on the new free surface elevation onto the free surface boundary within the mean flow. After several time steps, typically on the order of 500, the grid is moved to match the free surface elevations while conforming to the surfaces that intersect the free surface, such as the hull of a ship or the sail of a submarine; and as the loosely coupled interaction between the free surface, the Navier-Stokes equations and the grid movement algorithm converges, the solution approaches the nonlinear free surface solution.

Governing Equations

In deriving the kinematic free surface boundary condition, the free surface $\eta(x,y,z,t) = 0$ is considered as a material surface (i.e., no flow travels through the surface), so

$$\frac{D\eta}{Dt} = 0 \tag{12}$$

or

$$\frac{\partial \eta}{\partial t} + (u - V_x)\frac{\partial \eta}{\partial x} + (v - V_y)\frac{\partial \eta}{\partial y} + (w - V_z)\frac{\partial \eta}{\partial z} = 0 \tag{13}$$

By making the assumption that the free surface η can be expressed as $\eta(x,y,z,t) = y - Y(x,z,t) = 0$, this equation reduces to

$$\frac{\partial Y}{\partial t} + (u - V_x)\frac{\partial Y}{\partial x} - (v - V_y) + (w - V_z)\frac{\partial Y}{\partial z} = 0 \tag{14}$$

At steady-state, the kinematic boundary condition becomes

$$\begin{aligned} (\vec{u} + a_t) \cdot \left(\frac{\partial Y}{\partial x}, -1, \frac{\partial Y}{\partial z} \right) &= 0 \\ (\vec{u} + a_t) \cdot \alpha \hat{n}_{fs} &= 0 \end{aligned} \tag{15}$$

where $\alpha = \sqrt{1 + \left(\frac{\partial Y}{\partial x}\right)^2 + \left(\frac{\partial Y}{\partial z}\right)^2}$, so the flow is tangent to the free surface at steady-state.

The pressure in the numerical simulation at the free surface is set based on the free surface elevation. For the original, dimensional equations, the pressure at the free surface is the atmospheric pressure P_∞. Using the nondimensionalization, $P = \frac{P^* + \rho_\infty g y^* - P_\infty}{\rho_\infty U_\infty^2}$ with $P^* = P_\infty$ and $\frac{y^*}{L} = Y$, the pressure is clearly set to $P = \frac{Y}{Fr^2}$, where the Froude number is $\frac{U_\infty}{\sqrt{gL}}$.

Numerical Approach for Free Surface

The kinematic equation for the linear free surface is solved via a Galerkin finite element approach. In this approach, an algebraic equation is obtained for each node j by multiplying the governing equation by a weight function $\varphi_j(x,z)$, approximating the terms in the governing equation by using linear and bilinear interpolating functions $\phi_i(x,z)$ and integrating over the computational domain, or

$$\begin{aligned} \int_\Omega \varphi_j(x,z) \Bigg(\frac{\partial \tilde{Y}}{\partial t} + \left(\tilde{u} - \tilde{V}_x\right) \frac{\partial \tilde{Y}}{\partial x} - \left(\tilde{v} - \tilde{V}_y\right) \\ + \left(\tilde{w} - \tilde{V}_z\right) \frac{\partial \tilde{Y}}{\partial z} \Bigg) = 0 \end{aligned} \tag{16}$$

where the interpolated free surface elevation is $\tilde{Y}(x,z) = \sum_i Y_i \phi_i(x,z)$ and the velocities are of the form $\tilde{u}(x,z) = \sum_i u_i \phi_i(x,z)$.

For the triangular elements, the resulting equations are integrated using 7 point Gauss quadrature, and for the quadrilateral elements, the integrals are solved using 6 point Gauss quadrature in both directions. A first-order backward time discretization of Equation (16) is used for the temporal derivative, where $\frac{\partial \tilde{Y}}{\partial t} = \frac{\tilde{Y}^{n+1} - \tilde{Y}^n}{\Delta t}$ and the spatial terms evaluated at time level $n+1$. This discretization results in a linear algebraic system of the form $\Re_{fs}(Y^{n+1}, Y^n) = 0$. Since these equations are linear in the unknown variable Y_i^{n+1} at each time level (i.e., the velocities are frozen), the Jacobian matrix is calculated only once per time level. A Gauss-Seidel iterative solver similar to the one used to solve the discretized Navier-Stokes equations is used to identify the solution of the kinematic free surface equation by solving

$$\left[\frac{\partial \Re_{fs}}{\partial Y^{n+1}}\right] \Delta y^{n+1,m} = -\Re_{fs}(Y^{n+1,m}, Y^n) \qquad (17)$$

where $Y^{n+1,m+1} = Y^{n+1,m} + \Delta y^{n+1,m}$ and $Y^{n+1} = Y^{n+1,m+1}$ when $\|\Delta y^{n+1,m}\| <$ tolerance.

Within the viscous boundary layer, special care is needed in solving the kinematic free surface equation. On viscous surfaces, the flow velocity plus the grid velocity (i.e., $\vec{u} + a_t$) is set to zero, which prevents the free surface from moving at the viscous surface. Physically, however, surface tension effects force the free surface to rise and fall along the viscous surfaces. Since the solver does not simulate surface tension, another method must be employed to move the free surface near the viscous surfaces. Following the method used in the structured solver, the free surface at a certain distance from the viscous surface is extended at a constant height to the viscous surface. This distance is typically on the order of 2×10^{-4} times the characteristic length L, whereas the point spacing off of the viscous surface is on the order 10^{-6} for model scale simulations and 10^{-8} for full scale simulations.

Free Surface Boundary Condition

At the free surface boundary, the pressure is set to the hydrostatic pressure of $P = \frac{Y}{Fr^2}$. Determining the velocity to impose on the boundary is more difficult. If the velocity were forced to be tangent to the free surface (i.e., $(\vec{u} + a_t) \cdot \hat{n}_{fs} = 0$), then the free surface equation would reduce to $\frac{\partial Y}{\partial t} = 0$, and the free surface could not evolve. Thus, this tangency condition is relaxed to allow the free surface to evolve.

This boundary condition is implemented using a characteristic variable boundary condition, similar to the derivation used for the farfield boundary condition. For hyperbolic systems, flow information travels along characteristics; and for three-dimensional incompressible flow, three characteristics originate upstream, and one originates downstream. If the flow is traveling out of the domain (i.e, $(\vec{u} + a_t) \cdot \hat{n} > 0$), then only one characteristic needs to be specified from the outside, which is derived from the hydrostatic pressure. If the flow is traveling into the domain, three characteristics need to be specified from the outside. The characteristic variables are derived from considering the inviscid fluxes across the the boundary face, via

$$\frac{\partial Q}{\partial t} + \nabla F \cdot \hat{\vec{n}} = 0 \qquad (18)$$

where $\hat{\vec{n}}$ is the normal to the grid for each boundary face. The inviscid flux term can be rewritten as

$$\nabla F = \frac{\partial F}{\partial Q} \nabla Q = R \Lambda R^{-1} \nabla Q \qquad (19)$$

where Λ is a diagonal matrix with the eigenvalues Θ, Θ, $\Theta + c$ and $\Theta - c$, where $\Theta = u\hat{n}_x + v\hat{n}_y + w\hat{n}_z + a_t$ and $c = \sqrt{\left(\Theta - \frac{a_t}{2}\right)^2 + \beta}$. Premultiplying by R^{-1},

$$R^{-1} \frac{\partial Q}{\partial t} + \Lambda R^{-1} \nabla Q \cdot \hat{\vec{n}} = 0 \qquad (20)$$

Freezing the matrix $R_o^{-1} = R^{-1}(Q^{in})$,

$$\frac{\partial R_o^{-1} Q}{\partial t} + \Lambda \nabla \left(R_o^{-1} Q\right) \cdot \hat{\vec{n}} = 0 \qquad (21)$$

Using the definition $W(Q) = R_o^{-1} Q$, Equation (18) decouples into four equations for the four characteristic variables W as

$$\frac{\partial W}{\partial t} + \Lambda \nabla W \cdot \hat{\vec{n}} = 0 \qquad (22)$$

Three of the characteristics are obtained from upstream values, and one of the characteristics is obtained from downstream values. In the case of a boundary face, there are a set of characteristics associated with the inside flow $W^{in}(Q^{in})$ and a set of characteristics associated with the outside flow $W^{out}(Q^{out})$. The flow variables on the boundary face are determined from the appropriate characteristic variables via $Q = R_o W$. For flow traveling out of the domain, the characteristic

variables are chosen to be

$$W = \begin{bmatrix} w_1^{in} \\ w_2^{in} \\ w_3^{in} \\ w_4^{out} \end{bmatrix} \tag{23}$$

because the fourth eigenvalue $\Theta - c$ is negative, while the other eigenvalues are positive. For flow traveling into the domain, only the third eigenvalue is positive, so the characteristic variables are chosen as

$$W = \begin{bmatrix} w_1^{out} \\ w_2^{out} \\ w_3^{in} \\ w_4^{out} \end{bmatrix} \tag{24}$$

For farfield boundary conditions, the characteristic variables associated with the outside flow are taken as the freestream variables. For free surface boundary conditions, the characteristic variables for the outside flow are determined from the hydrostatic pressure and the only available velocity information, which is the velocity on the inside. However, this velocity is modified by removing a portion of the velocity component that is not tangent to the grid, via

$$\vec{u}^{out} = \vec{u} - \gamma((\vec{u} + a_t) \cdot \hat{n})\,\hat{n} \tag{25}$$

where

$$\gamma = \begin{cases} -(\vec{u} + a_t) \cdot \hat{n} & \text{if} \quad -1 \le (\vec{u} + a_t) \cdot \hat{n} < 0 \\ 1 & \text{if} \quad (\vec{u} + a_t) \cdot \hat{n} < -1 \end{cases} \tag{26}$$

When γ is 1, the velocity imposed from the outside is tangent to the grid (i.e., $\vec{u^{out}} \cdot \hat{n} = 0$). When the velocity was not modified or constrained in some fashion, the free surface algorithm became unstable for flow into the domain due to the inconsistency of using downstream information. This instability was a severe difficulty for the transom stern of Model 5415, but was not a difficulty for previous cases such as the Wigley Hull and Series 60. This modification provides enough control over the velocity to maintain stability of the algorithm, and if the grid is allowed to move to match the free surface, then this modification ensures that the flow will be tangent to the free surface at convergence. When using the grid speed terms a_t, such as for the constant turning case, the grid speed terms are not restricted via equation (25), only the velocity $\vec{u}^{out}$ is restricted.

Grid Movement Algorithm

After several time steps, the grid is moved to match the free surface while conforming to any solid surfaces intersecting the free surface, with displacements on the surface being propagated into the volume grid. Several methods are available for this grid movement, including the use of a Laplacian solver to propagate the surface perturbations into the volume grid, the use of a linear spring analogy where each edge is a spring whose stiffness is determined by the length of the edge, a torsional/linear spring analogy (Farhat, 1998) where the angle between the edges affects the stiffness of the springs in the mesh, or solving the linear elasticity equations to propagate the perturbations within the grid. The spring analogy is computationally efficient but is not robust. Both the spring analogy and the Laplacian solver generate elements with negative volumes for moderate amounts of movement, on the order of the size of 3 to 4 elements. Solving the linear elasticity equations to move the grid is robust, but the computational cost associated with this method is the primary drawback.

Thus, following the work of Farhat and extending it to three dimensional grids, the torsional/linear spring analogy has been developed and applied to the problem of moving the grid to match the linear free surface elevations. For tetrahedral grids, this method is quite robust, allowing severe distortions on the surface while maintaining positive volume elements. In practice, this algorithm allows up to approximately 80% compression of elements. Within the boundary layer, (i.e., near the viscous surfaces), the grid moves the same as the points on the boundary. This grid movement method is computationally costly but provides excellent robustness for the free surface solver.

The linear spring method for moving an unstructured grid is presented in (Batina, 1989) where each edge in the grid is replaced by a linear spring whose stiffness is inversely proportional to the length of the edge. Unfortunately, this method often fails for complicated geometries and for large changes in the boundary, because negative areas are generated when a node crosses over an edge in the grid. The creation of negative areas is illustrated in Figure 1, where node 1 is pushed downwards and node 4 is forced to cross the edge between nodes 2 and 3.

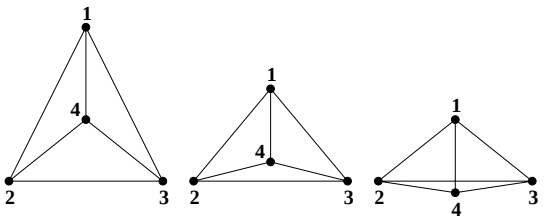

Figure 1. Negative Areas Produced by Linear Spring Method.

The reason for this failure is that the stiffness in the linear spring method prevents two nodes from colliding but does not prevent a node from crossing over an

edge. As two nodes get closer together, the stiffness increases without bound preventing the collision; but there is no mechanism to prevent a node from crossing an edge, because these crossovers can occur without the stiffness increasing without bound.

To provide a more robust movement algorithm for unstructured grid, Farhat developed an algorithm to prevent a node from crossing an edge by using torsional springs around each node, as shown in Figure 2.

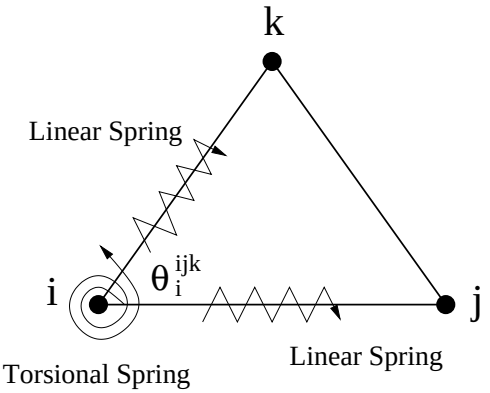

Figure 2. Placement of Linear and Torsion Springs.

The stiffness of the torsion spring C_{ijk} is inversely proportional to the sine of the angle, so that the stiffness grows without bound as the angle decreases towards zero or increases towards 180^o, or

$$C_{ijk} = \frac{1}{\sin^2 \theta_i^{ijk}} \tag{27}$$

where θ_i^{ijk} is the angle centered at node i formed from the edges ij and ik. Thus, as a node moves towards an edge, the angle goes towards zero, and the stiffness of the torsion spring grows. The sine of the angle is squared to prevent a negative stiffness. In addition, multiplying the stiffness by term that is inversely proportional to the distance to the viscous surfaces (Murayama, 2002) further improves robustness and is used here as well.

Farhat has derived the equations for the torsional spring methods for two-dimensional grids and provides an iterative solution method. In the present work, these methods have been extended into three dimensions, which provides an adequate level of robustness for the grid movement algorithm. The derivations of the three-dimensional torsional spring equations are beyond the scope of this paper and will be presented elsewhere.

The grid movement algorithm is implemented via several steps, with the goal of moving the grid to match the free surface while conforming to any geometry that intersects the free surface, such as a hull. These steps are described below:

1. Move nodes along surface to surface edges. There are several different types of edges, depending on each surface's relationship to the free surface. The nodal locations are determined based on the type of edge. For instance, an edge that lies fully within the free surface has its y-component determined by the free surface value, but its x and z-components are determined by the surface's relationship to the free surface. If the surface is projected in the z-direction, then the z-component is determined by this projection, while its x-component is determined by any stretching at the endpoints. When this process is attempted across several processor blocks, moving nodes in the edges becomes quite complicated.
2. Move nodes in the surface. Based on the displacements at the edges of each surface, the nodes in the surface are moved via torsional springs. Before this is attempted, however, the nodes must be projected onto a planar surface, requiring that each surface be "projectible", such that the surface can be uniquely projected onto a plane in some constant direction.
3. Once the nodes are moved in the projected surface, they must be projected onto a background surface representing the geometry. This background surface is significantly more resolved than the grid, and this background surface must extend above the original waterline, so as to allow for motion of the free surface above the waterline.
4. Move surface displacements into the prismatic, boundary layer grid, along boundary layer lines originating at each node in the viscous surface.
5. Move nodes in the volume based on surface displacements in all coordinate directions

EXAMPLES

These examples demonstrate the changes in the free surface profiles and the forces on the hull for changes in the grid resolution as well as for changes in incoming flow angles and for changes in the turning radius. The results from the grid refinement study indicate that the general features of the flow are obtained for each grid, but that the level of grid refinement has not reached the "grid independent" level, in that changes in grid refinement generates a noticeable change in the free surface from one grid to the next. Furthermore, the vortical structures under the hull change even more dramatically from one grid to the next, which is beyond the scope of this report.

These simulations were completed on an in-house LINUX cluster consisting of 1,024 processors, which consists of 1.0 GHz and 1.266 GHz Pentium III processors, with approximately 1.0 Gigabytes of RAM for each pair of processors. The grids are partitioned

such that approximately 100,000 nodes are in each partition. Hence, the largest grid is partitioned into 50 pieces to run on 50 processors.

Much of the work in this paper is based on lessons learned from simulations completed through the Department of Defense High Performance Computing (HPC) Challenge Project, including computational time on the IBM-SP3 at the Naval Oceanographic Office MSRC, the IBM-SP3 at the Maui High Performance Computing Center and the Cray T3E at U. S. Army Engineer Research and Development Center MSRC (Kim,2003)

Grid Refinement Study

The free surface flow around the DTMB Model 5415 Series hullform was simulated for six viscous grids with different point spacings, in order to determine the appropriate level of grid refinement for accurate free surface simulations and force and moment predictions. No attempt was made in the grid refinement study to insure that the grids were geometrically similar, in that control volumes were consistently divided from grid level to the next. In each grid level, the overall grid spacing was reduced by a factor of 0.8. By reducing the point spacing at the controlling points within the geometry, the point spacing on the surfaces and within the volume were also reduced by a similar amount. In addition, the point spacing in the stern region and along the hull behind the bow wave were further reduced, because of the sensitivity of these regions to changes in the point spacings. The size of each grid is shown in Table 1. The prisms are generated off of the viscous surfaces, which consist of triangular faces. The point spacing off of the viscous surfaces is selected to produce a $y+$ of approximately 1 on the viscous surfaces. The stack of prisms originating from each triangular face terminates when the aspect ratio of the prisms is approximately 1.0, so as the grid on the viscous surface is refined, the thickness of the prismatic region within the volume grid decreases. The effects of this boundary layer growth are outside the scope of this paper.

Grid Level	Nodes	Tetrahedra	Prisms
Viscous 1	477 K	891 K	603 K
Viscous 2	789 K	1,356 K	1,049 K
Viscous 3	1,184 K	2,383 K	1,459 K
Viscous 4	1,878 K	3,734 K	2,333 K
Viscous 5	2,563 K	6,377 K	2,759 K
Viscous 6	4,114 K	11,282 K	4,082 K

Table 1. Grid Sizes for Grid Refinement Study.

The force in the x-direction (i.e., drag) for each grid are tabulated below and are divided into three different parts, the force based on the dynamic pressure (Dyn. P), the force based on the hydrostatic pressure (Hydro. P) and the viscous force (Visc. Drag). The hydrostatic pressure force is defined herein as the surface integral of the vertical location y divided by the square of the Froude number dotted into the normal direction, over the viscous surface $\partial\Omega$, or

$$\int_{\partial\Omega} y\hat{n}dS \tag{28}$$

The hydrostatic pressure force is similar to the pressure attributable to the weight of the water on the surface. For fully-submerged objects, such as a submarine, this integral is equivalent to the weight of the displaced fluid and points in the downward direction. However, for surface vessels, the free surface may cause a non-zero component in the other directions, as well.

The viscous component is the primary influence in the drag, but the hydrostatic pressure contribution represents approximately 10% of the drag, which are shown in Table 2. In order to predict this component, the free surface must be simulated. Furthermore, the free surface simulation also directly affects the dynamic pressure by changing the amount of the wetted surface area over which the dynamic pressure acts, and by changing the pressure distribution on these surfaces. The effects of the free surface on the viscous effects is much more subtle, especially in understanding how the free surface interacts with the vortical structures, changing their strength and location. The viscous drag drops slightly as the grid is refined, while the hydrostatic pressure contribution stays almost constant as would be expected since it only depends on the free surface profile at the hull. The dynamic pressure changes more, which is probably a result of changes of the free surface in the stern. These results are compared with the experimental results as published in the Gothenburg 2000 Proceedings.

Grid	Dyn. P	Hydro. P	Visc. Drag	Total
1	2.160	0.887	4.214	7.261
2	1.889	0.812	4.105	6.806
3	1.643	0.816	4.088	6.547
4	2.222	0.850	3.820	6.892
5	2.340	0.810	4.028	7.178
6	2.520	0.882	3.824	7.226
Exp.	1.36	na	4.93	6.29

Table 2. Force in x-Direction (i.e., drag) $\times 10^4$.

The free surface for this sequence of grids is shown in Figures 3 and 4, which highlight the bow wave peak and trough and the stern. The height of the bow wave is approximately the same for each grid, although it does vary within a banded range, similar to the error bars for the experimental solution. The profile in the

bow trough also varies from one grid to the next, indicating that the grids are not in the "grid asymptotic" range, where changes in the grid do not change the result significantly. In the bow region, the free surface is reasonably symmetric, since the port and starboard sides are almost indistinguishable.

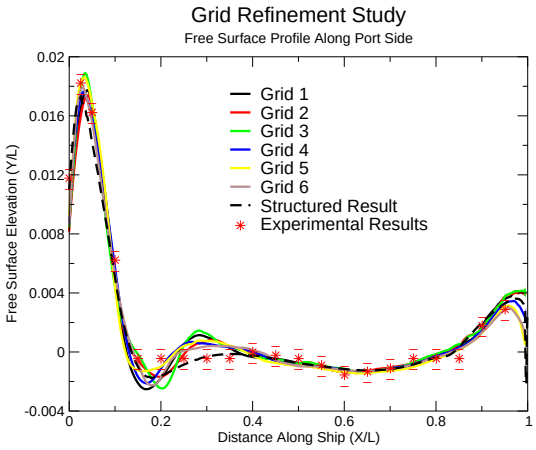

Figure 3. Comparison of Free Surface Profiles Along Port Side.

But in the stern, the free surface is not symmetric, even though every effort has been made to insure symmetry. The reason for this asymmetry is the interaction between the free surface, the grid movement algorithm and the turbulence effects. Slight asymmetries in the free surface cause the free surface grid to become asymmetric once the grid is moved to match the free surface. This asymmetry in the grid causes the free surface to become more asymmetric, which begins to affect the vortical structures underneath the ship. Once these asymmetries exist in the vortical structures, the free surface is completely altered, aligning with the vortical structures. Returning the free surface to a symmetric flow state after this asymmetry has set up is quite challenging. Also, in the stern profile, the elevations for the first three grids is significantly higher than for the last three grids. As can be seen from the roughness of the curve, the resolution in the stern region for the first three grids is not enough to capture the flow features. For the last three grids, much effort has been made to ensure that the grid along the free surface is symmetric, which affects the wave elevations. These simulations have not yet converged, due to asymmetries in the vortical structures. The drag is very sensitive to the free surface profile in the stern region, and since the free surface in the stern is not yet converged, the forces fluctuate greatly.

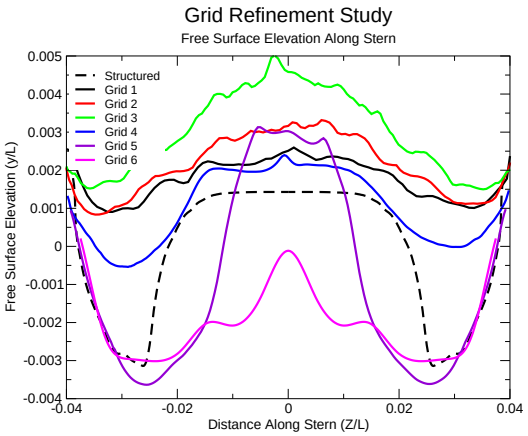

Figure 4. Comparison of Free Surface Profiles Along Stern.

In Figure 5, the vortical structure underneath the Model 5415 and the free surface contours showing the bow and stern waves are shown. These results are from the most refined grid, Grid 6. The vortex shed from the bulbous bow can be clearly seen for much of the length of the hull. In the stern, the vortical structure is quite complicated and is not symmetric, which adversely affects the symmetry of the free surface. As stated above, the interaction between the free surface, the grid movement algorithm and the vortical structures is quite complicated and prevents truly symmetric flow. The free surface contours show that the stern wave and the bow wave continue downstream of their originations.

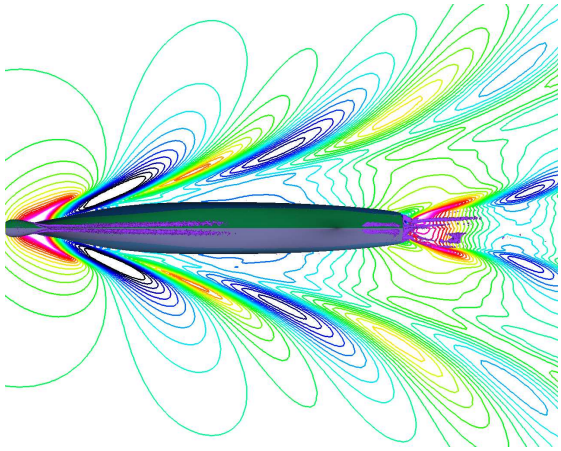

Figure 5. Free Surface Contours and Vortical Structure for Grid 6.

Angles of Drifts

Two different steady-state maneuvers were simulated for the DTMB Model 5415 series hullform. The

first maneuver was flow coming at the hull at different angles of yaw, simulating the effects of the ship drifting into the flow. The sink and trim were different for these simulations and hence the forces will not agree with those listed above. For this simulation, the grid was a symmetric grid, consisting of 4.8 million nodes, with 4.6 million prisms and 14.1 million tetrahedra, which is more resolved that Grid 6 in the refinement study. The goal of these simulations was to determine whether the free surface algorithm, and especially the grid movement algorithm, could satisfactorily capture the free surface in the bow and stern regions. In the bow region, the bow wave grows to an excessive height, whereas in the stern region, the free surface is quite complicated. Six different angles of drift were simulated, from 0 degrees to 5 degrees of yaw. As the angle of drift increases, the side force grows dramatically. At 0 degree angle of drift, the flow should be symmetric, so that the side force should be zero. Special effort has been made to enforce symmetry for the 0 degree case, which adversely affected the dynamic pressure for the drag, and even with this special effort, symmetric flow has not quite been achieved. The forces in the x-direction (i.e., drag) and in the z-direction (i.e., side-force) are shown in Tables 3 and 4. The change in the forces in Table 3, especially the viscous drag which comes from the skin friction, varies monotonically with a change in the angle. The slight drop in the dynamic pressure for Angle 4 may be a result of an under converged solution.

Angle	Dyn. P	Hydro. P	Visc. Drag	Total
0	2.252	0.821	4.406	7.479
1	2.742	0.907	4.423	8.072
2	2.811	0.956	4.440	8.207
3	2.876	1.045	4.462	8.383
4	2.823	1.172	4.479	8.474
5	3.122	1.335	4.507	8.964

Table 3. Force in x-Direction (i.e., drag).

The contributions to the side force are primarily from the difference in the dynamic pressure and hydrostatic pressure on the starboard and port sides of the hull caused by the flow approaching the ship at an angle. These forces scale linearly with the angle for the smaller angles and then they grow faster than linearly as the angle increases. As the flow angle increases, the ship's silhouette changes and the flow features change. For small angles, this change can be represented by a perturbation from flow at a 0 degree angle of yaw, but for larger angles, the flow patterns are significantly different, resulting in greater forces.

Angle	Dyn. P	Hydro. P	Vis. Drag	Total
0	0.062	0.006	0.007	0075
1	2.382	0.757	0.033	3.172
2	4.832	1.527	0.075	6.434
3	7.272	2.334	0.133	9.739
4	9.891	3.162	0.167	13.220
5	12.934	4.079	0.199	17.212

Table 4. Force in z-Direction (i.e., Side-Force).

The free surface along the hull is shown in the following figures along the port (Figure 7) and starboard side (Figure 8) and along the stern (Figure 9). The flow is approaching from the starboard side, which results in highly bow waves on the starboard side. The change in the free surface profiles for the bow wave are almost linear on both the port and starboard sides, not only at the bow but also along the entire length of the ship. The deflections in the stern are also as expected, showing a gradual change from the symmetric flow. The image for the stern region shows results from a previous simulation, which is more converged than the solution on the current grid, but used a different version of the free surface algorithm. For these simulations, the free surface algorithm and the grid movement algorithm are adequate for the free surface distortions.

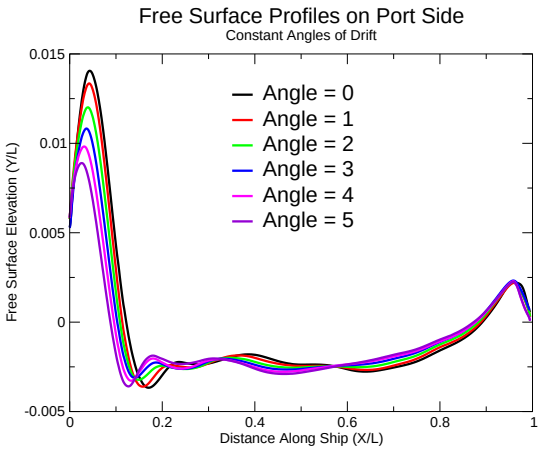

Figure 7. Free Surface Profiles Along Port Side.

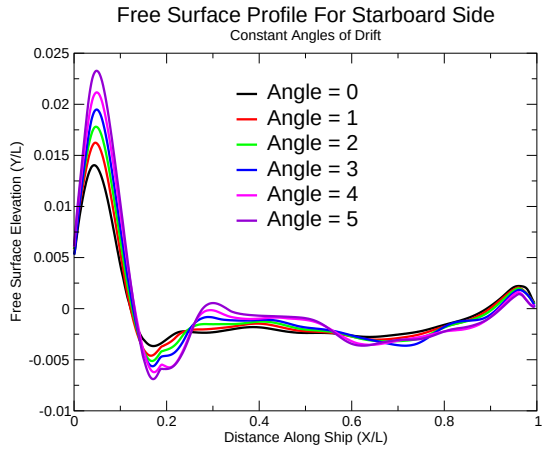

Figure 8. Free Surface Profiles Along Starboard Side.

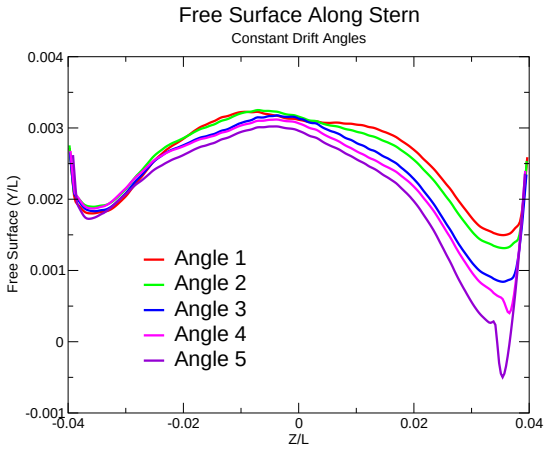

Figure 9. Free Surface Profiles Along Stern.

Finally, the vortex originating from the bulbous bow is shown in Figure 10, as well as the free surface contours for the bow wave and the stern wave. This image is for the case of the 5 degree turn.

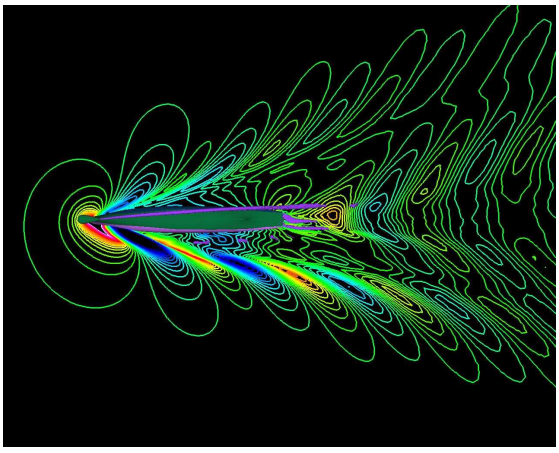

Figure 10. Free Surface Contours and Vortical Structure for Angle 5.

Constant Turning Radius

The second steady-state maneuvering case involved simulating the flow around the DTMB Model 5415 series hullform in a constant turn, with turning radii of 6, 12 and 24 times the hull length. For the tightest case, involving the turn of radius 6 times the hull length, the flow at the bow has an angle of approximately 5 degrees with the axis of the ship. For this simulation, the grid speed terms are non-zero while the farfield conditions are set to zero, so different aspects of the code are tested. The grid used for this simulation had a similar number of nodes as Grid 4 in the grid refinement study, but it differed in the placement of these points.

Radius	Dyn. P	Hydro. P	Visc. Drag	Total
24 L	2.481	1.057	4.135	7.673
12 L	2.581	1.113	4.146	7.84
6 L	2.951	1.452	4.220	8.623

Table 5. Force in x-Direction (i.e., drag).

The forces generated by these simulations are given in Table 5 and 6, showing the force in the x-direction, which is akin to drag, and the force in the z-direction, which is the side force. For the force in the x-direction, the viscous drag varies only slightly as the turning radius gets tighter, but the dynamic and hydrostatic pressure contributions increase as the turning radius decreases, indicating that the ship experiences greater drag through a tighter turn. The two pressure contributions to the side force approximately double as the turning radius halves, and the viscous force contribution to the side force is minimal.

Radius	Dyn. P	Hydro. P	Visc.	Total
24 L	-2.249	-1.113	0.002	3.360
12 L	-4.482	-2.234	0.016	6.700
6 L	-9.457	-4.703	0.035	-14.125

Table 5. Force in z-Direction (i.e., Side-Force).

The free surface profile along the port and starboard sides are shown in Figure 11. As would be expected, the free surface rises on the starboard side, which is the side turning into the flow and drops on the port side. As was the case with the angles of drift, the free surface profiles vary continuously with the change in the radius of the turn.

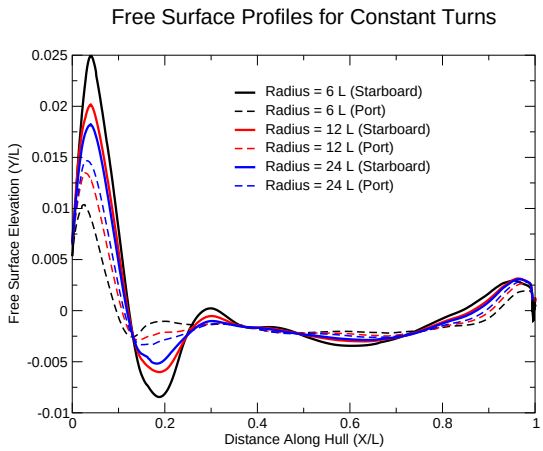

Figure 11. Free Surface Profiles along Port and Starboard.

Finally, the vortical structure and the free surface contours are shown in Figure 12. The vortical structure arising from the bulbous bow is quite strong and continues far downstream of the bow as it curves with the rotation of the ship. There is a strong vortex that originates at one corner of the stern and curves in response to the rise and fall of the free surface. The free surface also curves with the rotation of the ship.

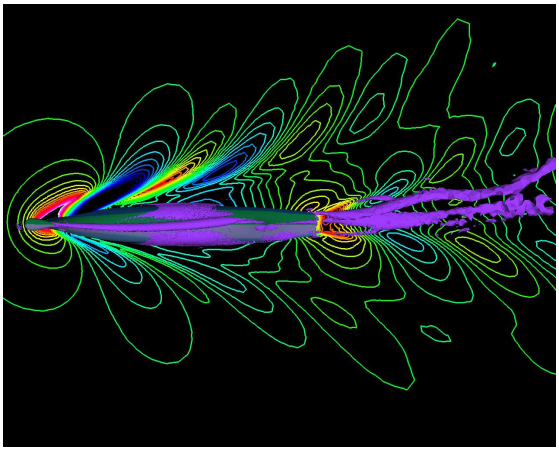

Figure 12. Free Surface Contours and Vortical Structure for Radius 6 L Turn.

Prescribed Linear Free Surface Maneuver

For the final case, the Model 5415 hullform is forced through a prescribed maneuver to study the free surface through a maneuver. The data for the maneuver was generated by using a rudder-induced, propulsor-driven 3 DOF maneuver for the Model 5415 without a free surface. In this simulation, the free surface was simulated as a symmetry plane, so that the free surface effects could be ignored. A fully-appended geometry of the Model 5415 was used, with the propulsors rotating to power the ship and with the rudders deflecting through the turn. The time step was 0.0002068 seconds per iteration, with each iteration taking approximately 60 seconds, and there were 3230 iterations in the maneuver. The ship turns to approximately 8 degrees from the original angle and reaches an angle with the incoming flow direction of slightly more than 6 degrees.

For the simulation presented herein, a steady-state simulation is performed with the ship traveling straight and level before the maneuver begins. This simulation does not have the rudders, propulsors or appendages, but the free surface is activated. The grid is not moved through the maneuver due to the computational cost and the probable instabilities associated with moving the grid frequently, but the grid at the beginning of the simulation is moved to match the steady-state free surface for the incoming flow.

For the case of the constant angles of drift, the simulation was performed by changing the flow direction at the farfield boundaries, hence imposing the angle of drift into the simulation. For the case of constant turning radii, a different aspect of the code was used, which involved the grid speed terms $a_t = -(V_x\hat{n}_x + V_y\hat{n}_y + V_z\hat{n}_z)$ while setting the farfield velocities to zero. These grid speed terms were constant throughout the simulation. For the case of the prescribed maneuver, the grid speed terms again were enabled, but they varied through the simulation as the ship performed its maneuver. Hence, this test case exercised a different portion of the code.

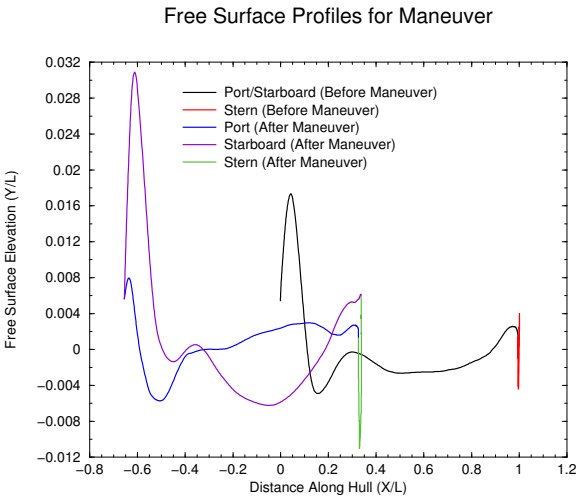

Figure 13. Free Surface along Hull for Maneuver.

One of the goals of this simulation was to determine how high the free surface would be along the hull. In Figure 13, the free surface along the hull before the maneuver and after the maneuver is shown. The free surface on the starboard side rises dramatically as the ship turns to starboard, while the free surface on the port drops off quite dramatically. Furthermore, the free surface profile along the ship's hull is

quite different, inducing a significant force imbalance from the starboard to the port side. And even though the ship reaches only an angle of only slightly more than 6 degrees with the incoming flow, the free surface rises to a height significantly higher than for the 5 degree drift case or the case with the tightest turning radius. For this case, the grid was fixed and was not allowed to conform to the free surface. If the grid were moved, then the free surface would probably become even more extreme, and may approach the limit of the grid movement algorithm to match the free surface.

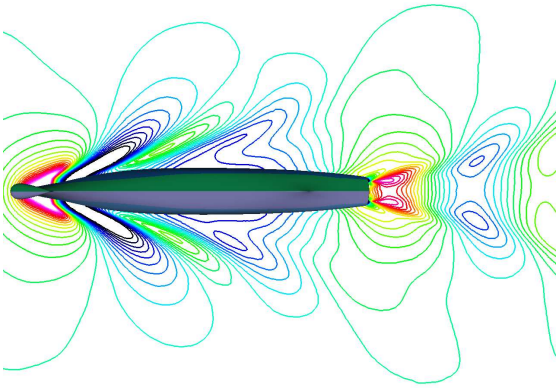

Figure 14. Free Surface Contours Before Maneuver.

The primary goal of this simulation, beyond determining whether the free surface elevations would grow too large for the grid movement algorithm, was to see whether the free surface would respond properly as the grid was rotated to match the ship's maneuver. In this maneuver, the entire grid was rotated and translated with the ship, as it moved. However, the free surface behind the ship should not rotate with the ship or the grid because it should not feel the effects of the rotation, but rather, the free surface should stay relatively fixed in relation to the original location of the ship. In other words, once the wave has left the ship, the behavior of the ship should not affect the wave. The free surfaces at the beginning and the end of the maneuver are shown in Figures 14 and 15, respectively. The free surface in Figure 14 is nearly symmetric about the centerline, but it does have some level of asymmetry, as discussed above. In Figure 15, the free surface aft of the ship again has some asymmetries, due to the asymmetries in the original free surface, but the free surface has not rotated with the ship or the grid, but remains in its original orientation.

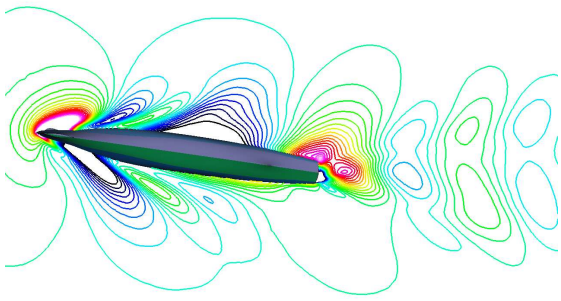

Figure 15. Free Surface Contours Before Maneuver.

CONCLUSIONS

A robust nonlinear free surface algorithm has been implemented within an unstructured finite volume flow solver of the the turbulent three-dimensional Reynolds-averaged Navier-Stokes equations. The free surface algorithm is a surface tracking algorithm which moves the grid to match the free surface while conforming to the hull and is loosely coupled to the flow solver via a characteristic variable boundary condition imposition of the free surface pressure distribution. This boundary condition implementation also enforces flow tangency along the free surface at convergence. Current simulations also indicate that the free surface algorithm is applicable to rotating and translating grids.

Results from a grid refinement study for the DTMB Model 5415 barehull form are provided which indicate that even more resolution is needed for a grid independent solution to be obtained. A discussion of the hydrostatic pressure force is provided which is an additional force not observed for fully-submerged simulations such as for a submerged submarine or for an aircraft in flight.

Several initial simulations progressing towards a true 6-degree-of-freedom (6-DOF) rudder-induced, propeller-driven maneuver in unsteady seas were completed, including various angles of drift up to 5 degrees and constant turns of various turning radius, with turns into the flow of up to 5 degrees, and one prescribed maneuver. The goal of these simulations was to determine whether the free surface algorithm could model such moderate maneuvers, in that the free surface would stay attached to the stern and that the grid movement algorithm could move the grid for such extreme grid motions, especially in the bow region. For the angle of drift and the constant turn cases, the free surface profiles gradually change over the spectrum of runs, as do the force predictions. In addition, the vortical structures respond to the changes in the flow conditions as expected. For the prescribed maneuver,

with fixed grid, the free surface contours that are aft of the ship do not rotate as the ship turns, which is physically realistic, and the vortical structures again behave appropriately.

These successful steady-state and linear free surface maneuvering simulations indicate that this approach to modeling the free surface can be useful for fully-appended, powered and self-directed 6-DOF maneuvers. Previous work has shown that the grid generation algorithm and the flow solver along with the free surface can build grids and simulate flow for fully-appended cases with rotating propulsors and at both model and full-scale Reynolds numbers. Continued research is needed to analyze, implement and test a fully-unsteady nonlinear free surface boundary condition implementation as well as to improve the computational efficiency of the grid movement algorithm so that the grid can be moved more frequently. Studies of the impact of moving the grid at each time step are also needed. Finally, a better understanding of the choice of turbulence model is needed, with the hopes that changing the turbulence model will improve the force predictions.

ACKNOWLEDGMENT

This research was sponsored by the Office of Naval Research with Dr. L. Patrick Purtell grant monitor and with Ki-Han Kim as the project leader for the HPC Challenge Project. This support is gratefully acknowledged.

REFERENCES

Anderson, W. K., and Bonhaus, D. L., "An Implicit Upwind Algorithm for Computing Turbulent Flows on Unstructured Grids", Computers in Fluids, Vol. 23, No. 1, Jan, 1994, pp. 1-21.

Batina, J. T., "Unsteady Euler Airfoil Solutions Using Unstructured Dynamic Meshes", 27th AIAA Aerospace Sciences Meeting, AIAA Paper 89-0115, Reno, Jan, 1989.

Beddhu, M., Taylor, L. K., and Whitfield, D. L., "A Time Accurate Calculation Procedure for Flows with a Free Surface Using a Modified Artificial Compressibility Formulation", Applied Mathematics and Computation, Vol. 65, 1994, pp. 33-48.

Beddhu, M., Jiang, M. Y., Taylor, L. K., and Whitfield, D. L., "Computation of Steady and Unsteady Flows with a Free Surface Around the Wigley Hull", Applied Mathematics and Computation, Vol. 89, 1998, pp. 67-84.

Beddhu, M., Jiang, M. Y., Whitfield, D. L., Taylor, L. K., and Arabshahi, A., "CFD Validation of the Free Surface Flow Around DTMB Model 5415 Using Reynolds Averaged Navier-Stokes Equations", Proceedings of the Third Osaka Colloquium on Advanced CFD Applications to Ship Flow and Hull Form Design, 1998.

Beddhu, M., Nichols, S., Jiang, M. Y., Sheng, C., Whitfield, D. L., and Taylor, L. K., "Comparison of EFD and CFD Results of the Free Surface Flow Field about the Series 60 C_B = 0.6 Ship", Proceedings of the Twenty-Fifth American Towing Tank Conference, 1998.

Beddhu, M., Jiang, J. Y., Whitfield, D. L. and Taylor, L. K., "Computation of the Wetted Transom Stern Flow over Model 5415", Proceedings of the Seventh International Conference on Numerical Ship Hydrodynamics, 1999.

Beddhu, M., Pankajakshan, R., Jiang, M. Y., Taylor, L., Remotique, M. G., Briley, W. R., and Whitfield, D. L., "Computation and Evaluation of CFD Results for Practical Ship Hull Forms", Proceedings of Gothenburg 2000: A Workshop on Numerical Ship Hydrodynamics, 2000.

Burg, C. O. E., Sreenivas, K., Hyams, D., and Mitchell, B., "Unstructured Nonlinear Free Surface Solutions: Validation and Verification", Proceedings of the 32nd AIAA Fluid Dynamics Conference and Exhibit, AIAA Paper 02-2977, June, 2002.

Burg, C. O. E., Sreenivas, K., Hyams, D., and Mitchell, B., "Unstructured Nonlinear Free Surface Simulations for the Fully-Appended DTMB Model 5415 Series Hull Including Rotating Propulsors", Proceedings of the 24th Symposium on Naval Hydrodynamics, July, 2002.

Chorin, A. J., "A Numerical Method for Solving Incompressible Viscous Flow Problems", Journal of Computational Physics, Vol. 2., 1967, pp. 12-26.

Coakley, T. J., and Hsieh, T., "A Comparison Between Implicit and Hybrid Methods for the Calculation of Steady and Unsteady Inlet Flows", Proceedings of the 21st AIAA/SAE/ASME/ASEE Joint Propulsion Conference, AIAA Paper 85-1125, July, 1985.

Farhat, C., Degand, C., Koobus, B., and Lesionne, M., "Torsional Springs for Two-Dimensional Unstructured Fluid Meshes", Computer Methods in Applied Mechanics and Engineering, Vol. 163, 1998, pp. 231-245.

Haselbacher, A., McGuirk, J. J., and Page, G. J., "Finite Volume Discretization Aspects for Viscous Flows on Mixed Unstructured Grids", AIAA Journal, Vol. 37, No. 2, Feb, 1999, pp. 177-184.

Hyams, D. G., Sreenivas, K., Sheng, C., Briley, W., R., Marcum, D. L., and Whitfield, D. L., "An Investigation of Parallel Implicit Solution Algorithms for Incompressible Flows on Multielement Unstructured Topologies", Proceedings of the 38th AIAA Aerospace Sciences Meeting and Exhibit, AIAA Paper 2000-0271, Jan, 2000.

Hyams, D. G., Sreenivas, K., Sheng, C., Nichols, S., Taylor, L., K., Briley, W. R., and Whitfield, D. L., "An Unstructured Multielement Solution Algorithm for Complex Geometry Hydrodynamic Simulations", Proceedings of the Twenty-Third Symposium on Naval Hydrodynamics, Sept, 2000.

Kim, K.-H., Gorski, J., Miller, R., Wilson, R., Stern. F., Hyman, M., and Burg., C., "Simulation of Surface Ship Dynamics", Proceedings of DOD High Performance Computing Modernization Program 2003 Users Group Conference, June, 2003.

Marcum, D. L., "Unstructured Grid Generation Using Automatic Point Insertion and Local Reconnection", The Handbook of Grid Generation, edited by J. F. Thompson, B. Soni and N. Weatherill, CRC Press, 1998, Section 18.

Murayama, M., Natahashi, K., and Matsushima, K., "Unstructured Dynamics Mesh for Large Movement and Deformation", Proceedings of the 41st AIAA Aerospace Sciences Meeting and Exhibit, AIAA Paper 02-0122, Jan, 2002.

Ratcliffe, T. J., and Lindenmuth, W. T., "Kelvin Wake Measurements Obtained for Five Surface Ship Models", DTRC 89-038, Jan, 1990, David Taylor Model Basin.

Ratcliffe, T. J., "An Experimental and Computational Study of the Effects of Propulsion on the Free Surface Flow Astern of Model 5415", Proceedings of the Twenty-Third Symposium on Naval Hydrodynamics, Sept, 2000.

Roe, P. L., "Approximate Riemann Solvers, Parameter Vectors and Difference Schemes", Journal of Computational Physics, Vol. 43, pp. 357-372, 1981.

Spalart, P. R., and Allmaras, S. R., "A One-Equation Turbulence Model for Aerodynamic Flows", AIAA Paper 92-0439, 1992.

Taylor, L. K., "Unsteady Three-Dimensional Incompressible Algorithm Based on Artificial Compressibility", PhD Thesis, Mississippi State University, 1991.